9020–9032 *Nucleic Acids Research, 2013, Vol. 41, No. 19* *Published online 8 August 2013*
doi:10.1093/nar/gkt691

Contributions of the RAD51 N-terminal domain to BRCA2-RAD51 interaction

Shyamal Subramanyam[1,2,3], William T. Jones[3], Maria Spies[2,3,*] and M. Ashley Spies[3,4,*]

[1]Department of Biochemistry, University of Illinois Urbana-Champaign, Urbana, IL 61801, USA, [2]Center for the Physics of Living Cells, University of Illinois Urbana-Champaign, Urbana, IL 61801, USA, [3]Department of Biochemistry, Carver College of Medicine, College of Pharmacy, University of Iowa, Iowa City, IA 52242, USA and [4]Division of Medicinal and Natural Products Chemistry, Department of Pharmaceutical Sciences and Experimental Therapeutics, College of Pharmacy, University of Iowa, Iowa City, IA 52242, USA

Received March 26, 2013; Revised July 12, 2013; Accepted July 15, 2013

ABSTRACT

RAD51 DNA strand exchange protein catalyzes the central step in homologous recombination, a cellular process fundamentally important for accurate repair of damaged chromosomes, preservation of the genetic integrity, restart of collapsed replication forks and telomere maintenance. BRCA2 protein, a product of the breast cancer susceptibility gene, is a key recombination mediator that interacts with RAD51 and facilitates RAD51 nucleoprotein filament formation on single-stranded DNA generated at the sites of DNA damage. An accurate atomistic level description of this interaction, however, is limited to a partial crystal structure of the RAD51 core fused to BRC4 peptide. Here, by integrating homology modeling and molecular dynamics, we generated a structure of the full-length RAD51 in complex with BRC4 peptide. Our model predicted previously unknown hydrogen bonding patterns involving the N-terminal domain (NTD) of RAD51. These interactions guide positioning of the BRC4 peptide within a cavity between the core and the NTDs; the peptide binding separates the two domains and restricts internal dynamics of RAD51 protomers. The model's depiction of the RAD51-BRC4 complex was validated by free energy calculations and *in vitro* functional analysis of rationally designed mutants. All generated mutants, $RAD51^{E42A}$, $RAD51^{E59A}$, $RAD51^{E237A}$, $RAD51^{E59A/E237A}$ and $RAD51^{E42A/E59A/E237A}$ maintained basic biochemical activities of the wild-type RAD51, but displayed reduced affinities for the BRC4 peptide. Strong correlation between the calculated and experimental binding energies confirmed the predicted structure of the RAD51-BRC4 complex and highlighted the importance of RAD51 NTD in RAD51-BRCA2 interaction.

INTRODUCTION

Human RAD51 and BRCA2 proteins are the key contributors to genomic integrity and are of a paramount importance to the cell. The intricate choreography of molecular events orchestrated by these two proteins ensures accurate and timely progression of homologous recombination (HR) (1,2) and has an important additional function at the replication fork [reviewed in (3)]. HR repairs genotoxic DNA lesions via precisely coordinated DNA transactions that lead to exchange of information between two homologous DNA molecules (4) and play a prominent role in faithful duplication of the genome (4) and telomere maintenance (5). DNA Repair by HR depends on assembly of the RAD51 recombinase into a dynamic nucleoprotein filament on single-stranded DNA (ssDNA) generated at the site of damage or collapsed replication (4,6–8). Assembly of the RAD51 filament is tightly regulated and requires assistance from a recombination mediator (9,10). One of these recombination mediators in human cells, 3148 amino acid (aa) BRCA2, is a tumor suppressor protein, which mediates HR by recruiting RAD51 to sites of the DNA double-strand breaks and facilitates loading of the RAD51 protein onto resected ssDNA coated with Replication protein A (RPA) ssDNA-binding protein (11,12). Once formed, the presynaptic RAD51 nucleoprotein filament promotes homology search and the DNA strand exchange reaction (2,11–13). Mutations in human BRCA2 protein cause a predisposition to breast and ovarian cancers and increase susceptibility to other tumorigenic conditions (14,15).

BRCA2 interacts with RAD51 through a series of eight motifs called BRC repeats and a separate binding site

*To whom correspondence should be addressed. Tel: +1 319 353 5645; Fax: +1 319 335 9570; Email: michael-spies@uiowa.edu
Correspondence may also be addressed to Maria Spies. Tel: +1 319 335 3221; Fax: +1 319 335 9570; Email: maria-spies@uiowa.edu

located in the C-terminal region (2,7,10,16). The highly conserved BRC repeats, ~35 aa in length, are variably spaced in a segment of the protein encoded in exon 11 of the *BRCA2* gene (17,18). Although all BRC repeats of BRCA2 promote RAD51 nucleoprotein formation, the modes of their interaction are split among two classes based on their affinities for RAD51 versus the RAD51 ssDNA filament (19). Among eight BRC repeats involved in RAD51 binding, BRC4 displays the highest affinity for RAD51 (19).

The interaction between BRC peptides and RAD51-family proteins likely represents a universal means of regulating (positively or negatively) the recombinase assembly and activity. A variant of BRC motif recently found in RECQL5 helicase plays a critical role in its anti-recombinogenic activity (20), whereas loading of bacterial RecA recombinase on the ssDNA by RecBCD helicase/nuclease involves interaction with the structural elements on the RecA/RAD51 core also critical for BRC4–RAD51 interaction (21). Although the interaction between BRCA2 and RAD51 is of a paramount importance, understanding of its structural basis is limited to the crystal structure of the core domain of RAD51 fused to the BRC4 peptide (22). The structure features two areas of hydrophobic interactions involving F1524 and F1546 of the BRCA2 and the core of RAD51 and has been exploited in design of the peptide inhibitors of BRC4–RAD51 interaction (23) and, more recently, in the identification of low molecular-weight fragments that display mM affinity with a goal of using them in a fragment-based approach (24). A relatively featureless binding interface between RAD51 core and BRC4 peptide consists of hydrophobic interactions that involve most of the BRC4 peptide. Additionally, the interface contains several polar interactions that provide a modest contribution toward peptide binding (22). As only the core of RAD51 is present in the structure, potential involvement of the missing N-terminal domain (NTD) is unclear.

Here, we combined homology modeling and molecular dynamics (MD) simulations to build an accurate atomistic description of the full-length RAD51 protein in complex with the BRC4 peptide. Our computational studies predicted previously unknown interactions between BRC4 peptide and the RAD51 NTD. Moreover, the structure and the position of the NTD differed significantly from that of the yeast Rad51 (25), used as a template for our model. The model's rendition of the complex was validated by *in silico* binding free energy calculations, and *in vitro* by the functional analysis of mutants designed based on the results of the computational studies.

MATERIALS AND METHODS

RAD51 homology model

The crystal structure of yeast Rad51 gain of function mutant [PDB ID: 1SZP, (25)] representing an active conformation of the Rad51 filament was used to build a homology model of two RAD51 monomers adjacent in the nucleoprotein filament. The model was constructed using The Chemical Computing Group's Molecular Operating Environment (MOE) (26). Ten intermediate homology models resulting from permutational selection of different loop candidates and side chain rotamers were built for RAD51, each subjected to a degree of energy minimization using the force field MMFF94x, with a distance-dependent dielectric. The model of the monomer (chain B) was constructed in the presence of the adjacent monomer in the 1SZP-A template, to optimize the monomer–monomer interface. The intermediate model that scored best according to the packing evaluation function was chosen for the next level of refinement: the RAD51 dimer was constructed by superposition of the RAD51 homology modeled monomer onto the 1SZP dimer crystal structure, followed by simulated annealing energy minimization and 4 ns MD simulations with the knowledge-based YASARA force field (vide infra).

The Mg-ATP substrate was placed by first building and then docking with flexible ligand docking into a region that corresponds to the canonical ATP binding site of the *Escherichia coli* RecA protein [PDB ID: 1XMS, (27)]. The AutoDock implementation in YASARA Structure was used. AutoDock 4 uses a Lamarckian genetic algorithm to sample ligand conformations and binding modes. It uses a semi-empirical free energy force field to predict free energies of binding, which accounts for intermolecular and intramolecular energies, as well as charge-based desolvation. The following general docking parameters were used: 25 independent docking runs, each with a total of 2.5×10^6 energy evaluations, a torsional degrees of freedom value of 8, grid point spacing was left at the default of 0.375 Å, and the force field selected was AMBER03. Specific to the genetic algorithm, the following parameters were used: a population size of 150, 2.7×10^4 generations, an elitism value of 1, a mutation rate of 0.02 and a crossover rate of 0.8. Final poses were considered distinct if they varied by a Root Mean Squared Deviation (RMSD) of >5 Å. All atom energy minimization was then performed on the docked structure. This represented a starting point for MD simulations, and no constraints were placed on the Mg-ATP.

Placement and conformational search of BRC4 peptide

The partial structure of human RAD51 with BRC4 peptide (PDB 1N0W) was superposed onto the dimer Rad51 homology model using the superpose utility of MOE, to initially place the BRC4 peptide at the interface of the two monomers. The complex was then subjected to a specialized stochastic conformational search protocol called LowModeMD (28) within the MOE package. This method concentrates kinetic energy on low-frequency vibrational modes, to populate conformations in multiple low-energy states with high-computational efficiency, and is particularly appropriate for complex systems with large numbers of non-bonded interactions, such as peptides, peptide loops and macrocyles. The LowModeMD conformational search procedure includes an iterative process of initial energy minimization, filtering of high-frequency vibrational modes, a short (~0.5 ps) MD and saving distinct structures in a database. The energy minimization gradient threshold was 0.001 kcal/mol/Å, and

searches were configured to terminate after 200 contiguous failed attempts to generate novel conformations, with up to 10 000 iterations. Conformations were identified as unique if their root-mean-square-distance was above a threshold value of 0.75 Å. RAD51 protein remained frozen throughout the LowModeMD conformational search, and a single low-energy peptide conformation was identified.

Classical MD simulations with two adjacent RAD51 monomers

The MDs simulations on the homology model of RAD51 containing ATP and in the presence and absence of BRC4 peptide were performed with the YASARA Structure package version 12.4.1 (YASARA Biosciences—www.yasara.org). A periodic simulation cell with dimensions 104.94, 73.68 and 78.23 Å was used with explicit solvent. The YASARA knowledge-based force field (KBFF) was used with long-range electrostatic potentials calculated with the Particle Mesh Ewald method (29,30), with a van der Waals cutoff of 7.864 Å. This force field has been highly successful for use with homology modeling and protein structure prediction, in that it limits the damage (i.e. drifting into structurally unrealistic protein phase space) that often results from energy minimization and MD using empirical force fields.

ATP force field parameters were generated with the AutoSMILES utility (31), which uses semi-empirical AM1geometry optimization and assignment of charges, followed by assignment of AM1BCC atom and bond types with refinement using RESP charges, and finally the assignments of general AMBER force field atom types. The hydrogen bond network of RAD51 was optimized using the method of Hooft and coworkers (32), to address ambiguities from multiple side chain conformations and protonation states that are not resolved by the electron density of the template. YASARA's pKa utility was used to assign pKa values at pH 7.0 (33). The box was filled with water, with a maximum sum of all bumps per water of 1.0 Å and a density of 0.997 g/ml. The simulation cell was neutralized with NaCl (0.9% w/v final concentration). Excessive water molecules were deleted to readjust the solvent density to 0.997 g/ml. A short MD was run on the solvent only. The entire system was then energy minimized using first a steepest descent minimization to remove conformational stress, followed by a simulated annealing minimization until convergence (<0.05 kJ/mol/200 steps). The MD simulation was then initiated, using the canonical ensemble at 298 K, and integration time steps for intramolecular and intermolecular forces were calculated every 1.25 fs and 2.5 fs, respectively. This procedure was conducted after each *in silico* mutation as well. The structural alignments were performed with the MUSTANG method (34).

Free energy binding calculations with the fast boundary element method

The method used here is called the Boundary Element Method (BEM) (35,36). It falls under the class of free energy calculations known as Endpoint Methods, which also includes the popular Molecular Mechanics/Poison Boltzmann/Surface Area (MM-PBSA) approach (also called the finite difference method) (37). Endpoint Methods calculate the ΔG_{bind} from constituent parts of a thermodynamic cycle that involve solvation of the individual components. The binding energy expression is

$$\Delta G_{Bind,Solv} = \Delta G_{Bind,Vaccum} + \Delta G_{Complex,Solv} - \left(\Delta G_{Ligand,Solv} + \Delta G_{Receptor,Solv}\right) + \Delta G_{np}$$

In the BEM, much of the focus is placed on accurately representing the boundary between the two dielectrics, in which an accurate boundary charge distribution is used to represent a uniform dielectric at the interface between the low and the high dielectric continuum. From this boundary region of uniform dielectric strength, Coulomb's Law is used to calculate the electrostatic potentials.

A major difficulty in Endpoint Methods is assigning an internal dielectric (38). As the BRC-peptide binding cavity of RAD51 is relatively solvated, we chose to use a protein dielectric ε of 13; values of 4–20 are routinely used, often using mixed values (38,39). ΔG_{bind} values obtained from Endpoint Methods, such as MM-PBSA or BEM, should be viewed as enhanced scoring functions, which have enhanced rank-ordering value, rather than as metrics of accurate absolute binding free energy (40). For the current study, using BEM, the boundary between solvent (dielectric constant 78) and the solute (dielectric constant 13) was formed by the latter's molecular surface, constructed with a solvent probe radius of 1.4 Å and the following radii for the solute elements: polar hydrogens 0.32 Å, other hydrogens 1.017 Å, carbon 1.8 Å, oxygen 1.344 Å, nitrogen 1.14 Å, sulfur 2.0 Å. The solute charges were assigned based on the AMBER03 force field (41). The term for the hydrophobic component of peptide binding, ΔG_{np} was not included in these calculations, as this value is not expected to change in the mutated complexes being considered. The peptide binding entropy was not included in the relative binding energy calculations and is not expected to significantly contribute to this value. After a 1 ns equilibration period, BEM ΔG_{bind} value was calculated every 7 ps, for duration of 3 ns. The ensembles of the endpoint peptide binding free energy values were obtained for the wild-type RAD51, E42A, E59A, E237A, E59A/E237A and E42A/E59A/E237A mutants (Figure 5A) and transformed into the histograms (Figure 5B) using GraphPad Prism 4.

RAD51 protein expression and purification

RAD51 protein was expressed in *E. coli* Acella™ strain in the presence of pLysSRARE and pChaperone (generous gift from Dr Alex Mazin, Drexel University) plasmids in LB medium containing Carbenicillin (50 μg/ml), Kanamycin (40 μg/ml) and Chloramphenicol (34 μg/ml). The cells were grown at 37°C. After OD_{600} reached 0.6 RAD51 expression was induced with 0.1 mM IPTG (Calbiochem). Induced cells were further incubated at 37°C for 4 h, pelleted by centrifugation and lysed by sonication in the lysis buffer containing 100 mM Tris–OAc (pH 7.5), 2 mM EDTA, 10% Glycerol, 1 mM DTT,

Lysozyme (0.5 mg/ml), 0.1% Triton X-100 and Complete, mini, EDTA Free Protease Inhibitor Tablets (Roche). The clarified lysate was then dialyzed overnight against three changes of 0.5 l of 20 mM Tris–OAc (pH 7.5), 7 mM Spermidine, 10% Glycerol, 0.1 mM DTT. The precipitate was collected by centrifugation, re-suspended in T-75 buffer [50 mM Tris–HCl (pH 7.5), 10% Glycerol, 75 mM NaCl, 0.1 mM DTT] and then centrifuged again. The pellet and supernatant were collected, and the process was repeated by re-suspending the pellet in T-150, T-250, T-500 and T-600 buffers (containing 150 mM, 250 mM, 500 mM and 600 mM NaCl, respectively). Fractions containing RAD51 were pooled and loaded onto HiTrap Blue column equilibrated with Buffer BA [100 mM Potassium Phosphate (pH 7.0), 5% Glycerol, 300 mM NaCl, 1 mM EDTA, 1 mM DTT]. Protein was eluted using a 0–2 M Sodium Thiocyanate gradient and dialyzed overnight in Buffer HA [20 mM HEPES (pH 7.5), 5% Glycerol, 150 mM NaCl, 1 mM EDTA, 1 mM DTT]. RAD51-containing fractions were then loaded onto a Heparin column and protein eluted with a 150 mM – 2 M NaCl gradient followed by overnight dialysis in Buffer HA. Finally, the RAD51-containing fractions were concentrated on a MonoQ column using a steep 150 mM – 1.2 M NaCl gradient elution. The purified RAD51 was then dialyzed overnight in modified Buffer HA (0.1 mM EDTA), aliquoted and stored at −80°C. RAD51 concentration was determined using absorption at A_{280} with an extinction coefficient of $12800\,M^{-1}cm^{-1}$ (42). Percentage of glycerol in buffers could be varied between 5 and 10%. Human RPA was purified as previously described (43).

RAD51 E42A, E59A, E237A, E59A/E237A and E42A/E59A/E237A mutants were produced using the QuikChange II XL site-directed mutagenesis kit (Agilent) using the oligonucleotide primers described in the Supplementary Table S1. All mutants were purified using the protocol described for the wild type RAD51.

Fluorescence polarization anisotropy based RAD51-BRC4 binding assay

Binding affinity of RAD51 for the BRC4 peptide was measured by following fluorescence polarization anisotropy (FPA) of Fluorescein labeled BRC4 peptide (44). In all, 15 nM of FITC-BRC4 peptide (FITC-KEPTLL GFHTASGKKVKIAKESLDKVKNLFDEKEQ) (45) was incubated at 37°C in the reaction buffer containing [20 mM HEPES (pH 7.0), 2 mM $CaCl_2$, 10 mM $MgCl_2$, 1 mM DTT]. Fluorescence and fluorescence polarization anisotropy were measured using excitation and emission wavelengths of 490 and 518 nm, respectively, using Cary Eclipse Fluorimeter. Experiments were carried out in the presence of 1 mM ATP. Dissociation constants (K_d) were calculated by fitting the data to the binding isotherm–

$$\Delta A = \Delta A\,max \times \frac{\left\{(Kd + [RAD51] + [BRC4]) - \sqrt{(Kd + [RAD51] + [BRC4])^2 - 4[RAD51][BRC4]}\right\}}{2[BRC4]}$$

Where ΔA is change in anisotropy, ΔA_{max} is maximum change in anisotropy, [RAD51] is the total RAD51 concentration at each point of the titration and [BRC4] is the total peptide concentration. GraphPad Prism 4 software was used for the data analysis.

DNA binding and extension assay

The ability of RAD51 to bind and extend ssDNA was measured using Forster Resonance Energy Transfer (FRET)-based assay described previously (46). In all, 600 nM nucleotides (10 nM molecules) of dT_{60} oligo labeled with the Cy3 and Cy5 dyes separated by 25 nt was titrated with RAD51 protein in FRET Reaction Buffer [20 mM HEPES (pH 7.5), 150 mM KCl, 5 mM $CaCl_2$, 5 mM $MgCl_2$, 1 mM ATP, 1 mM DTT] at 37°C. Cy3 and Cy5 fluorescence was recorded using Cary Eclipse Fluorimeter. FRET was calculated as a fraction of acceptor intensity relative to the total donor and acceptor intensity adjusted by correction factors as described in (46).

RAD51 ability to extend DNA beyond the contour length was evaluated by comparing with the DNA extension by human RPA.

To observe the effect of the BRC4 peptide on nucleoprotein filament formation, a similar assay was performed by pre-forming the fully extended nucleoprotein filaments by mixing 400 nM of RAD51 with 10 nM molecules of dT_{60}. BRC4 peptide was then titrated into the reaction, and the resulting increase in FRET was calculated as described earlier in the text.

Images

Molecular graphics images were produced using the UCSF Chimera package from the Resource for Biocomputing, Visualization, and Informatics at the University of California, San Francisco [supported by NIH P41 RR-01081; (47)].

RESULTS

RAD51 homology model and BRC4 peptide placement

Saccharomyces cerevisiae Rad51 structure (PDB ID: 1SZP) (25) was used as a template to build a homology model of two adjacent protomers within human RAD51 filament (Figure 1).

Following all atom MD simulations with the KBFF, YASARA, ~60% of the RAD51 model (chain B) overlapped with the yeast Rad51 (1SZP-B) with the average RMSD between Cα atoms under 1.23 Å. Several parts of the structure, however, deviated significantly between the yeast and human proteins (Supplementary Figures S1A and S2A) and therefore were not recognized by the alignment algorithm, MUSTANG, which was used for the structure comparison and has a cutoff of 3.75 Å for the structurally similar residues to be matched (34). The most profound difference between the two structures involved the linker region between the NTD and the conserved core domain (Supplementary Figures S1A and S2A), which in the yeast Rad51 consists of two alpha helices connected by a flexible loop, whereas the NTD of human RAD51 is connected to the core by a long rigid

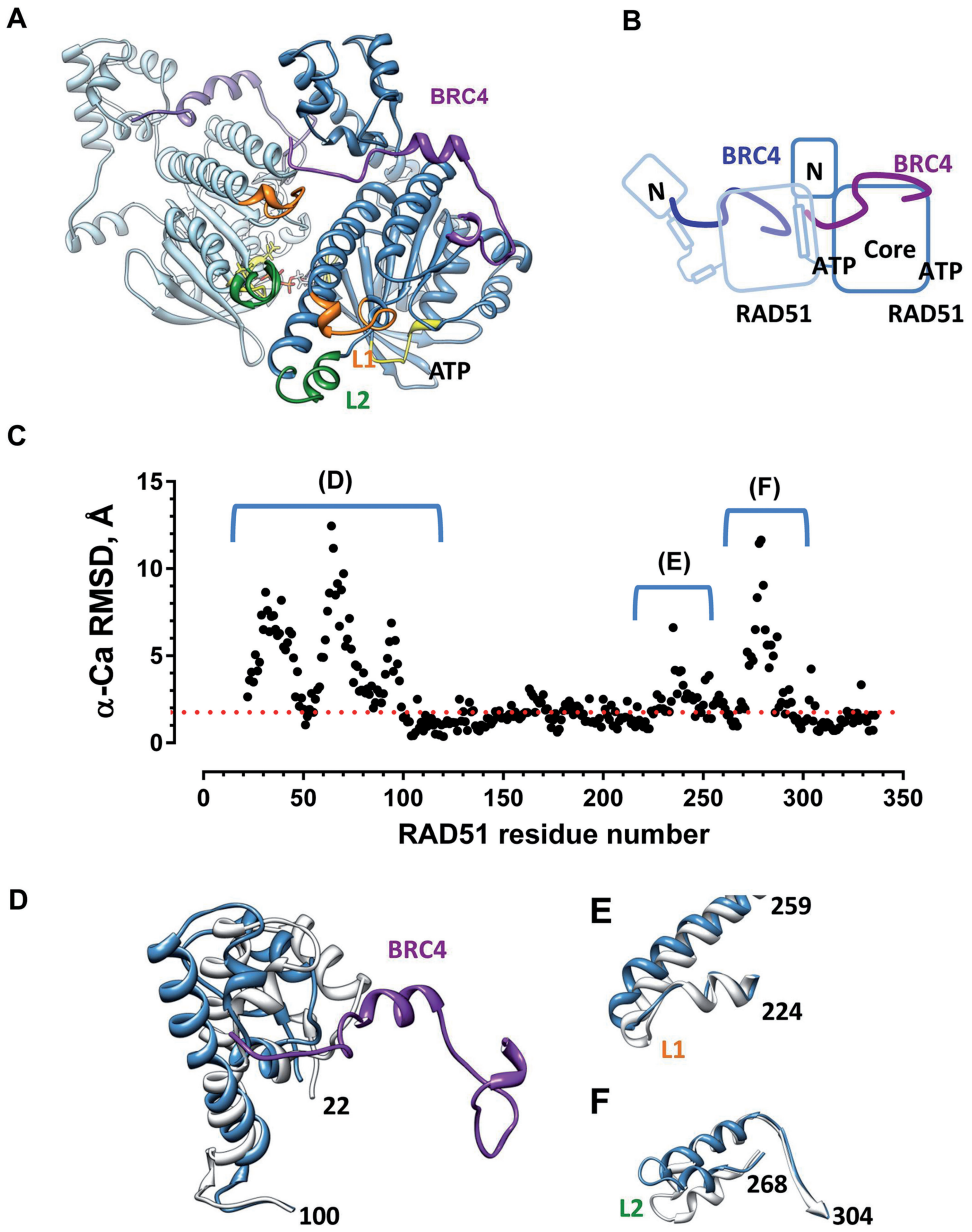

Figure 1. RAD51-BRC4 model and BRC4-induced structural rearrangements in RAD51 filament. (**A**) Ribbon diagram of the homology model of two adjacent RAD51 protomers containing BRC4 peptides: Chain B is shown in a dark blue; chain A is in a lighter blue; the two peptides are shown in purple. The RAD51 DNA-binding loops L1 and L2 are shown in orange and green, respectively, and the ATP binding region is shown in yellow. (**B**) Schematic representation of the BRC4 peptide bound RAD51. (**C**) α—Carbon RMSDs for the peptide-free and BRC4-bound RAD51 (chain B) as a function of the residue number. Letters D–F above the graph indicate the most divergent structural elements. The respective structural overlaps are shown in the panels (**D–F**) (D) NTD and the linker; (E) dsDNA-binding Loop L1; (F) ssDNA-binding loop L2.

helix. Although the overall 4 helix bundle structure of the NTD is preserved in the human protein, two of these helices display a slightly different orientation. These differences in the NTD and the linker region affect mainly chain B of RAD51 model whose NTD is located near the protomer–protomer interface. Structural change in the linker region and NTD also affected the overall orientation of the N terminal domain resulting in the wider cavity between the NTD and the core, which in RAD51 accommodates BRC4 peptide after a relatively small conformational change (Figure 1C–F, Supplementary Figures S1C and S2C show structural overlap between the peptide-free and the peptide-bound RAD51). Notably, we observed a remarkable overlap between our model and the crystal structure of the core RAD51 (1N0W), fused to BRC4 peptide of BRCA2 (22), which was not used in the model construction. Most of the structure (1N0W) overlapped with the homology model to yield an RMSD under 1 Å, with the exception of flexible areas around the DNA-binding loops, and several residues preceding the Walker A box. The overall RMSD for Cα atoms was 1.22 Å (Supplementary Figures S1B and S2B).

This provides valuable orthogonal information on the quality of the model, as 1N0W was not used to construct the homology model. The convergence between our model and 1N0W RAD51 core structure is especially remarkable, as these two structures share higher similarity than that observed between our modeled RAD51 and the structure of the yeast protein, which was used as a template to build the model.

Our RAD51 model scored well on a number of physical metrics. The Z-score, which evaluates the homology model for a set of physical parameters such as 3D packing, bond lengths, bond angles and so forth (48), after MD was −0.89, which means that the normality of 3D- and 1D-packing, as well as Ramachandran coordinates are <1 standard deviation from the gold standards from high-resolution crystal structures (48). Many other checks were also performed to ensure normality, including normality of van der Waals and Columbic energies = 0.557; planarity of peptide bonds = −0.215; normality of dihedral bonds = 0.08; normality of bond angles = 0.291; normality of bond lengths = 0.48; normality of water positions = −0.392; isomers = zero wrong isomers.

The placement of the BRC4 peptide in the RAD51 model was a critical step as the previously published crystal structure of RAD51 core in complex with BRC4 peptide had the peptide fused to the RAD51 core domain via a flexible linker (22). This posed some uncertainty with regard to the native complex in solution, and how it should be represented in MD simulations. Furthermore, absence of the NTD of RAD51 from the crystal structure allowed BRC4 peptide to partially occupy the spatial domain that should be occluded by the NTD.

First, we placed the peptide in the chain B. Owing to the inherent flexibility of the peptide, an exhaustive conformational search was performed using LowMode MD while keeping the protein coordinates static. LowMode MD is an accelerated MD method allowing configurational searches outside of the usually restrictive classical MD time scales, concentrating the kinetic energy on low frequency vibrational modes (see 'Materials and Methods' section) (28).

Finally, simulated annealing energy minimization and MD was performed with the YASARA KBFF, as described earlier in the text, (see 'Materials and Methods' section) (48). The second peptide was placed in the chain A by structural superposition of the subunit A of the homology model and the peptide, followed by simulated annealing energy minimization, as described in the MD methods section. Thus, we obtained a system of two monomers, each with a bound peptide. The motivation for placing the second peptide was to provide a greater degree of structural similarity to a multimeric system. Only the first peptide (placed in the chain B), which interfaces with a structurally complete binding site was used in the free energy calculations and pocket analysis and yielded insights that guided the experimental part of this study. Notably, the overall structure and position of this BRC4 peptide in the homology model was remarkably similar to that observed in the crystal structure (Supplementary Figure S2B). This was primarily achieved through a slight movement of the RAD51 NTD relative to the peptide free model (Supplementary Figures S1C and S2C).

Model of the RAD51-BRC4 complex predicts that both the core and NTD of RAD51 participate in the peptide positioning

Some structural rearrangements within RAD51 model were necessary to accommodate the BRC4 peptide (Figure 1C–F, Supplementary Figure S1C and S2C), which primarily involved movement of the NTD and the DNA-binding loops. The average RMSD between Cα atoms of the RAD51 core in the absence and presence of the peptide were 2 Å, whereas the average RMSD between Cα atoms of the NTDs were 4.9 Å. The NTD and the RAD51 core formed a cleft, which accommodates the C-terminal part of the BRC4 peptide (Figure 2A).

Several previously unknown interactions were predicted between RAD51 and the BRC4 peptide (Figure 2A). Notably, although most of these interactions involved the RAD51 monomer to which the peptide is placed (chain B), the model reveals additional contacts between BRC4 peptide and the adjacent monomer (chain A). The carboxylate of E237 defines the turn between the dsDNA-binding Loop 1 (49,50) and the N-terminus of α-helix 5 [in the nomenclature from (22)], by receiving a hydrogen bond from the backbone amide of S233. This feature results in the β-hydroxyl of S233 pointing into the peptide-binding pocket and acting as a hydrogen bond donor for the backbone carbonyl of E1548 and a hydrogen bond recipient of the backbone amide of this same residue. Simulations of the E237A mutant showed that the turn region of the adjacent monomer became less defined than the wild-type, resulting in the S233 group pointing away from the peptide binding cavity, and thus contributing to a decrease in the peptide binding free energy.

The NTD of RAD51 participates in the interaction as well: the carboxylate of E59 forms hydrogen bonds with the amide of N1544 and the amide of K1549 on the BRC4 peptide; the amide of K1543 bonds with the backbone carbonyls of A44 and E42. Within the same region, E42 interacts through hydrogen bonding with S26, which in turn stabilizes the secondary structure of the RAD51 NTD (Figure 2A). The average distance between the heteroatoms involved in these hydrogen bonds consistently remained below 3 Å during the course of a 3 ns MD simulation (Figure 2B).

In silico mutagenesis of three key glutamates (E42, E59 and E237) suggested their importance for correct positioning of the BRC4 peptide and predicted a network of interactions that the RAD51 NTD contributes toward the stable binding of the BRC4 peptide to RAD51 protein (Figure 2). MD simulations of RAD51 E42A and E237A mutants were used to analyze disruption of the hydrogen bonding interactions mentioned earlier. As expected, the distances between the involved heteroatoms increased markedly after the 4 ns MD of the mutants. Simulation results for E42A showed that the only

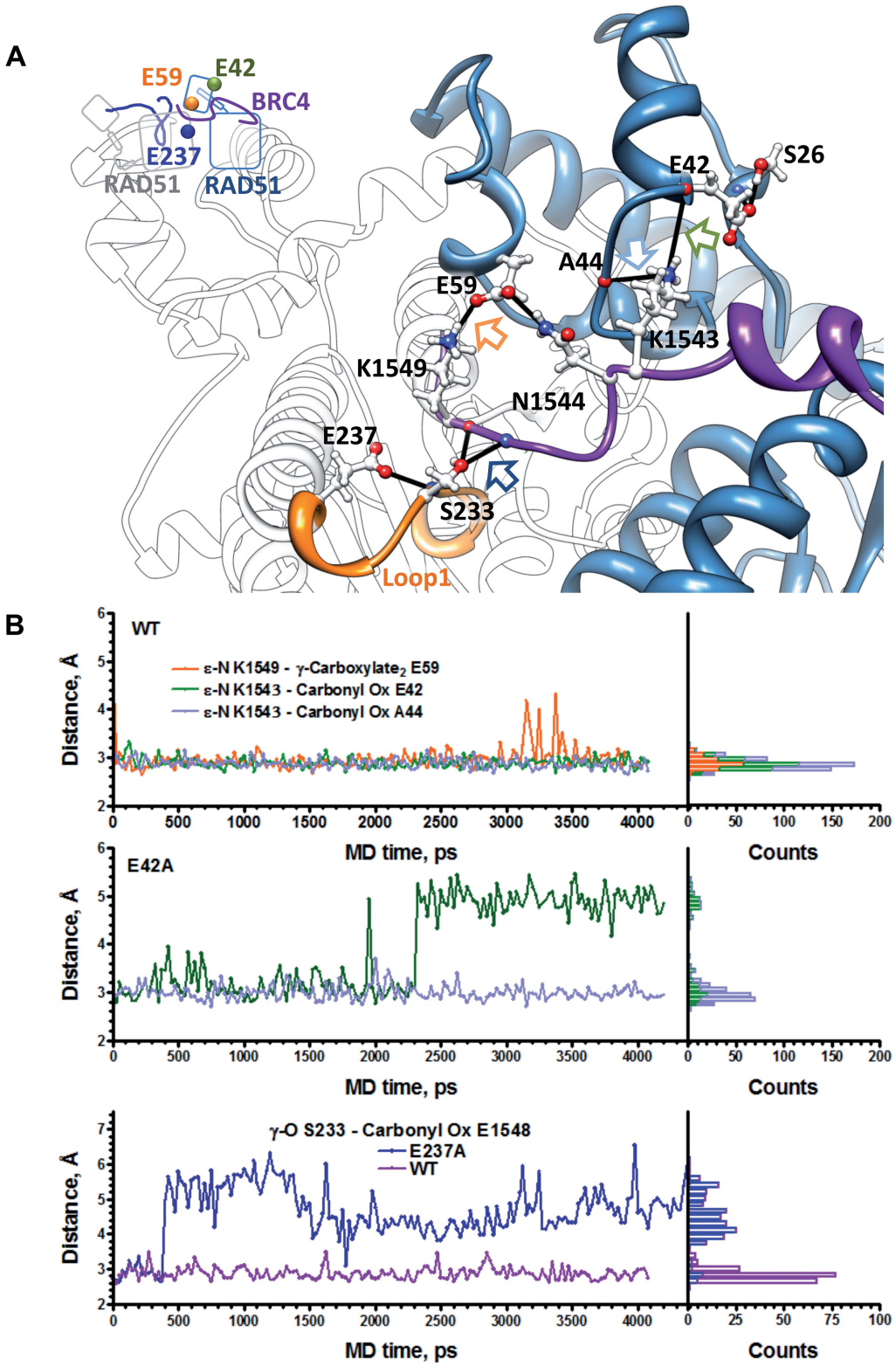

Figure 2. Non-obvious interactions involved in BRC4 positioning between the RAD51 core and NTD revealed by the model. (**A**) Interface between RAD51 (chain B is shown in blue, chain A is shown in white) and BRC4 peptide (purple). The key residues are represented in ball in stick. The key hydrogen bonds described in the text are shown as black lines. The colored arrows indicate hydrogen bonds followed over the MD simulation as shown in the panel (**B**). (B) Change in the distances between heteroatoms participating in the hydrogen bonds as functions of MD simulation time. The distances were extracted from the wild-type structure (top) and E42A mutant (middle); comparison of the wild-type and E237A (bottom). The distributions of the distances are also shown as histograms on the right.

hydrogen bonding partners left for K1543 are L41 and A42 backbone carbonyls, with heteroatom distance of ~3.0 Å; this is substantially different than the wild-type hydrogen bonding pattern in which every available hydrogen of the ε-nitrogen of K1543 is engaged in hydrogen bonding: 2.8 Å to carbonyl of A44, 2.8 Å to carbonyl of E42 and 3.0 Å to carbonyl of F46. Therefore, both E237A and E42A mutants yield predictable decreases in binding affinities toward the BRC4 peptide and predict a series of collective interactions that the RAD51 NTD contributes toward the stable binding of the BRC4 peptide to RAD51 protein (Figure 2A). These observations also suggested the mutant candidates for *in vitro* analysis of the contributions of the RAD51 NTD as well as for validation of our homology model.

RAD51 mutants retained structure and basic biochemical properties of the wild-type protein

Based on the predictions from the model, alanine mutants of three residues E42, E59 and E237 along with double mutant E59A/E237A and triple mutant E42A/E59A/E237A were constructed, purified and analyzed to validate the role of these residues in the RAD51-BRC4 complex (Supplementary Figures S3 and S4). If our model is sound, these amino acids should display reduced affinities toward BRC4 peptide without perturbing other biochemical activities and properties of RAD51. E237A was used to indirectly study the effect of S233, which is located in the dsDNA-binding loop (L1) and may be critical for RAD51 function. Analysis by circular dichroism spectroscopy confirmed that the three mutants maintained the secondary structure contents characteristic of wild-type RAD51 (Supplementary Figure S3D).

Formation of the recombination competent RAD51 nucleoprotein filament causes ~1.5-fold ssDNA extension over the B-form. Such filaments contain one RAD51 monomer per 3 nt of ssDNA and can be formed in the presence of ATP and Ca^{2+} ions (51,52). Both DNA extension and binding stoichiometry are indicators of the active nucleoprotein filament formation. DNA binding and extension activity was measured using a FRET-based assay wherein we observed and quantified the RAD51-mediated extension of dT_{60}, a 60mer ssDNA substrate labeled with the FRET donor (Cy3) and acceptor (Cy5) fluorophores separated by 25 nt (46,53,54). Under the stoichiometric-binding conditions, RAD51 titration results in gradual FRET decrease due to the spatial separation of the Cy3 and Cy5 fluorophores until the substrate is saturated with RAD51, and no further extension can be achieved. The inflection point in the titration curve reports on the binding stoichiometry, whereas the amplitude of the FRET decrease reports on the DNA extension (see 'Materials and Methods' section). Similar to the wild-type RAD51, all three mutants showed capacity to bind ssDNA with similar binding stoichiometries and to extend DNA (Supplementary Figure S4).

RAD51 mutants display reduced affinity for BRC4

As the three mutants retained structure and biochemical activities of the wild-type RAD51, they can be directly compared for their ability to bind BRC4 peptide. FPA was used to characterize binding of RAD51 mutants to the BRC4 peptide. Measurements were performed in the presence of ATP to closely reflect *in silico* studies. Protein was incrementally titrated into buffer containing FITC-labeled BRC4 peptide. Increase in FPA reflected RAD51–BRC4 complex formation (44). Binding isotherms were analyzed using a 1:1 binding equation, which assumes a single peptide binding site per monomer of RAD51 (see 'Materials and Methods' section. Because the signal follows the bound state of the peptide, this simple binding model is applicable for the FPA analysis even though the wild type RAD51 and the five mutants exist as broad distributions of oligomeric forms (Supplementary Figure S3C). In the presence of ATP, RAD51 bound BRC4 peptide with K_d of 34 ± 5 nM. As expected, all alanine mutants displayed reduced affinity for BRC4 peptide and bound with K_d values of 118 ± 16 nM, 397 ± 74 nM, 235 ± 39 nM, 208 ± 33 nM, 290 ± 57 nM for E42A, E59A, E237A, E59A/E237A and E42A/E59A/E237A mutants, respectively (Figure 3). The magnitude of the change in the FPA signal reflects the size of the complex containing fluorescence peptide. The E59A, E237A, E59A/E237A and E42A/E59A/E237A mutants displayed higher FPA changes compared with the wild-type RAD51 and the E42 mutant. This is likely due to binding of higher RAD51 oligomeric species to BRC4 and highlights importance of the contacts between the C-terminal end of BRC peptide and both adjacent monomers.

Altering interaction between S233 of RAD51 and E1548 of BRC4 peptide bound into the adjacent RAD51 monomer sensitizes RAD51 nucleoprotein filaments to dissociation by the BRC4 peptide

We pre-formed RAD51 nucleoprotein filaments on the Cy3 and Cy5 labeled ssDNA (dT_{60}) as described in the 'Materials and Methods' section. Under selected conditions (400 nM RAD51 per 600 nM nucleotides ssDNA), all mutants formed fully extended nucleoprotein filaments (Supplementary Figure S4). We then challenged the RAD51-ssDNA complexes by titrating in the unlabeled peptide (Figure 4). There is no clear agreement in the literature on how isolated BRC4 peptide affects RAD51-ssDNA nucleoprotein filament. Both negative (22,55–57) and positive (19,58) effects have been reported. Our experimental conditions were more similar to those reported in (57,59), in that we used a synthesized peptide, whereas Carreira and colleagues used Glutathione S-transferase-fused BRC4. Similar to (22,55–57), we observed destabilization of the extended RAD51 nucleoprotein filament. Nucleoprotein filaments formed by the wild-type and mutant RAD51 proteins are affected to a different degree by BRC4 peptide (Figure 4): BRC4 readily dissociated E237A, E59A/E237A and E42A/E59A/E237A mutants from ssDNA but only had a marginal destabilizing effect on the wild-type RAD51, E42A and E59A mutants.

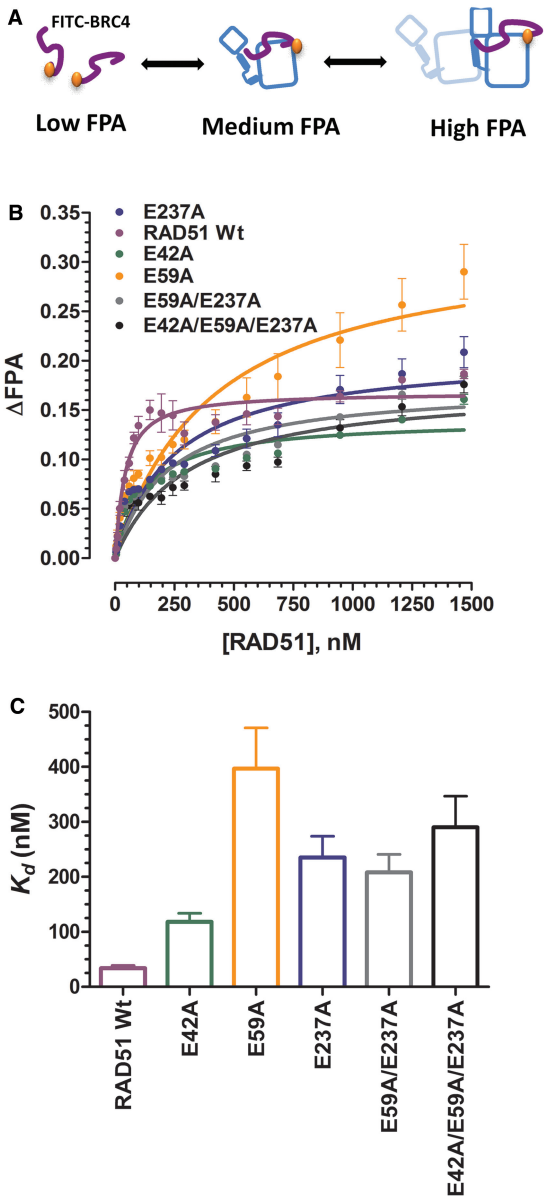

Figure 3. RAD51 mutants display compromised affinities for BRC4 peptide. (**A**) Schematic representation of the FPA-based peptide-binding assay. BRC4 peptide is shown in purple; FITC dye is in orange; RAD51 is in blue (**B** and **C**). Binding isotherms show titration of the 15 nM BRC4 peptide with the indicated concentrations of the wild-type and mutant RAD51 proteins. The K_d values are indicated by the respective isotherms. The error bars represent standard error (SEM) for three independent experiments; error bars are smaller than the data points where not seen.

The increased sensitivity of the three mutants containing E237A substitution to nucleoprotein filament disruption by BRC4 peptide is intriguing. It suggests that the S233-E1548 interaction disrupted by this mutation controls peptide access to the RAD51 monomer-monomer interface. It is also formally possible that the observed destabilization effect is due to the perturbed monomer-monomer interface. We disfavor this hypothesis, however, as the monomer–monomer interface appears intact in the post-MD structures of the mutants. These results do not contradict the high FPA signal

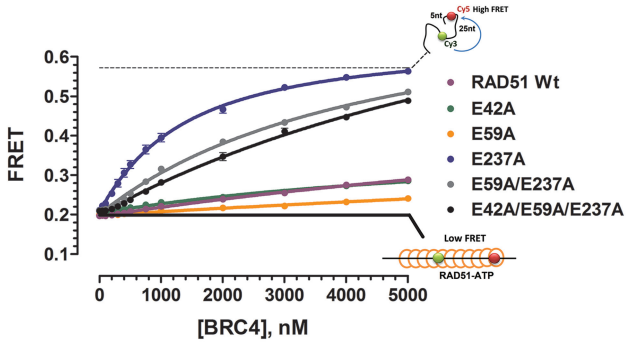

Figure 4. Nucleoprotein filaments respond differentially to BRC4 peptide challenge. Active RAD51 filaments were formed on a 60-mer oligonucleotide poly(dT)-60 labeled with Cy3 (FRET donor) and Cy5 (FRET acceptor) fluorophores separated by 25 nt. Addition of 400 nM RAD51 wild-type and mutants generated an extended nucleoprotein filament with a characteristic FRET value of ~0.2. Displacement of proteins from the oligonucleotide was inferred from an increase in FRET value on BRC4 peptide titration. Protein free oligonucleotide has a characteristic FRET value of ~0.6 under selected buffer conditions (see also Supplementary Figure S4).

observed for the E237A-BRC4 complexes: the high FPA signal is achieved at high protein:peptide ratio, whereas in the extension experiment, concentration of the RAD51 is fixed and the concentration of BRC4 peptide greatly exceeds that of RAD51.

Correlation between *in silico* and *in vitro* results reaffirm the role of RAD51 NTD

Endpoint free energy calculations were used to determine the relative $\Delta G_{binding}$ for peptide binding to RAD51 and were measured over the final 3 ns of the MD simulations, after an initial 1 ns pre-equilibration period (see 'Materials and Methods' section section). These binding endpoint free energy calculations exclude a number of terms such as ligand and receptor binding entropies and the non-polar interactions with solvent (i.e. cavitation and van der Waals interaction with solvent). Furthermore, the use of an implicit solvent model to calculate the changes in the solvation energies necessitates the use of a uniform dielectric constant, which strongly affects the magnitude of the calculated binding energy. However, such endpoint free energy calculations have been useful in accessing the relative changes in binding free energy (37,60,61).

The ΔG_{bind} trajectories for each protein (Figure 5A) were analyzed and converted into frequency histograms to yield the distributions of ΔG_{bind} values over the course of MD simulation (Figure 5B). These representations allow following small, but discernible differences in the computed binding energies. Relative ΔG_{bind} values derived from these distributions were compared with the respective relative ΔG values calculated from experimentally derived K_ds. All five mutants, E42A, E59A, E237A, E59A/E237A and E42A/E59A/E237A, showed average changes in ΔG_{bind} rank-ordered similarly to the experimentally derived values. The changes in computational binding energies correlate extremely well with free energy changes obtained empirically with an coefficient of determination (R^2) of 0.87 (Figure 6). An agreement

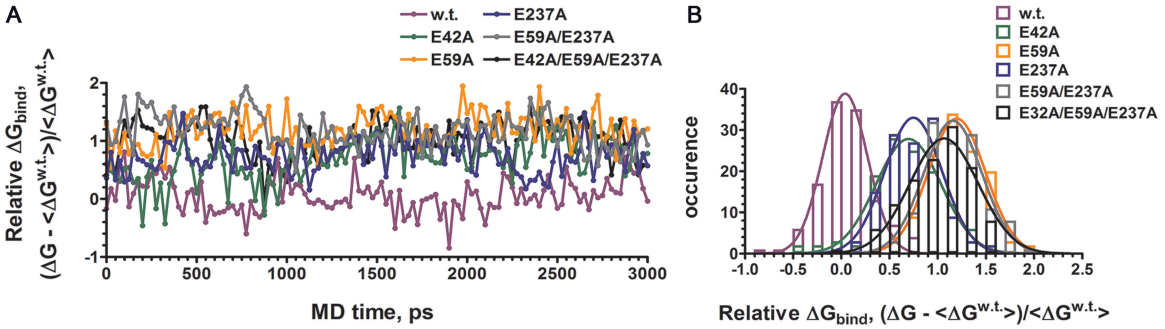

Figure 5. Computational binding energies ΔG_{bind} for the BRC4 interaction with wild-type RAD51, E42A, E59A, E237A, E59/E237A, E42A/E59A/E237A. (**A**) ΔG_{bind} trajectories for the BRC4 complex with each protein over the course of MD simulation. (**B**) Trajectories were converted into frequency histograms to yield the distributions of ΔG_{bind} values.

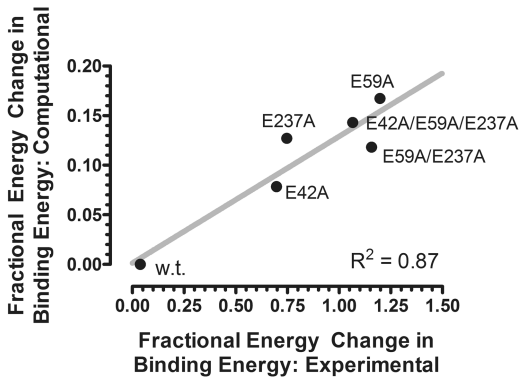

Figure 6. Correlation between computational and experimental relative binding free energies. Computational and experimental relative binding free energies show a high degree of correlation ($R^2 = 0.87$). This validates the protein–peptide interface of the RAD51–BRC4 homology model and the contributions of the RAD51 NTD toward BRC4 binding. Experimental fractional changes in binding energy were calculated from K_d values (Figure 3B). Computational fractional changes in binding energy were calculated using endpoint, BEM as $\langle \Delta G_{bind} \rangle = (\Delta G - \langle \Delta G_{w.t} \rangle)/\langle \Delta G_{w.t} \rangle$ (Figure 4).

between relative changes in free energy of binding validates the protein–peptide interface of the homology model and the contributions of the RAD51 NTD toward BRC4 peptide binding.

DISCUSSION

Proteins and enzymes orchestrating key steps in DNA repair are emerging as promising new targets in anticancer drug discovery, with RAD51 being one of the most attractive targets. Crucial for maintenance of genomic integrity in normal cells, RAD51 allows the transformed or cancerous cells to develop resistance to radiation and DNA-damaging drugs used in chemotherapy. Elevated levels of RAD51 lead to rapid accumulation of genetic variation, genomic instability, acquisition of invasiveness, drug and radiation resistance and disease progression in many cancers including Barrett's adenocarcenoma (62), multiple myeloma (63), recurrence of chronic myeloid leukemia (64), high grade gliomas (65) and lung cancer (66). Targeting RAD51 may therefore allow chemo- and radio-sensitization of cancerous cells as an adjuvant in standard combination anticancer regimens (67).

Several recent HTS campaigns and rational design of inhibitors/effectors of RAD51 were only mildly successful yielding an inhibitor of unknown mode of action with IC_{50} of 27.4 μM and poor drug-like properties (*log*P = 5 and low ligand efficiency of −0.23 kcal/heavy atom) (68); a small molecule that mildly stimulated RAD51-mediated strand exchange activity (69); DNA aptamers (70); peptide inhibitors (23) and most recently, an inhibitor of RAD51 filament formation that covalently binds to the RAD51 (71).

The existing high-resolution structure of the RAD51 core fused to the BRC4 peptide of BRCA2 tumor suppressor protein identified several key contacts between the two proteins, suggested the determinants of BRC4 peptide affinity for RAD51 and the mechanism by which it may affect the nucleoprotein filament (22). The identified contact areas on the RAD51 core surface, however, display poor druggability due to a featureless interaction surface (72) with only small pockets that bind phenylalanine (24). In contrast, the interface between the two adjacent RAD51 monomers within the filament and the cleft between the NTD and the RAD51 core may contain numerous loci that can be targeted.

Here, we report a model of RAD51, which includes both the NTD and the conserved core. Remarkably, the post-MD model converged with the structure of the RAD51 core (PDB ID: 1N0W), which was not used in the model building. The presence of the two monomers in the model allowed us to realistically represent the monomer–monomer interface within the RAD51 filament as well as the position of the NTD of one of the monomers (chain B). Such a representation is important considering the originally proposed role for BRC4–RAD51 interaction is to destabilize RAD51 oligomers in solution (55). Our model also predicted interactions between BRC4 peptide and the two RAD51 monomers adjacent in the filament. It, therefore, represents the initial stage of the RAD51–BRCA2 complex formation where the interface between adjacent monomers of RAD51 is slightly perturbed, but not yet completely abolished and replaced by the interactions with N-terminal

part of the BRC4 peptide. While the BRC4 peptides were placed in both monomers, contacts made by only one peptide placed in the chain B and contacting the monomer–monomer interface were evaluated. The backbone of the BRC4 peptide in our model overlapped well with the peptide in the 1N0W structure; the orientations of several side chains, however, were different reflecting their interactions with the NTD and the adjacent monomer. This was somewhat unexpected, as the position of the peptide in the crystal structure might have been constrained by fusion of the peptide to the RAD51 core and by extraordinary dense crystal packing. In our model, on the other hand, the NTD partially overlapped with the space occupied by the peptide in the crystal structure. Modeling of the RAD51–BRC4 complex suggested that the largest deviation between the RAD51 structures with and without the BRC4 peptide will involve movement of the NTD (Figure 1C and D, Supplementary Figures S1C and S2C).

To confirm the validity of the model, we identified several previously unknown contacts between the BRC4 peptide and RAD51. In particular, we focused on the contacts that involved the NTD or the adjacent RAD51 monomer. The binding energy calculations of the BRC4 complexes with the 3 RAD51 glutamate to alanine mutants carried out over 4 ns MD simulations suggested that the three following mutants, E42A, E59A and E237A, and their combinations should display compromised affinities for the BRC4 peptide, but retain the biochemical properties of the wild-type RAD51. Indeed, the five purified mutants had lower than the wild-type affinity for the BRC4 peptide with the rank order predicted by the binding energy calculations. As expected for hydrogen bond disruptions in a protein–peptide contact surface, the contributions from each of the identified residues to the overall energy of the RAD51–BRC4 complex formation are relatively modest. Loss of the binding energy predicted and confirmed for all mutants highlights the importance of the NTD of RAD51 in the BRC4 positioning. Combined, our data suggest the mechanism by which the interaction between BRC4 peptide and the adjacent monomer within the RAD51 oligomer contributes to the RAD51 oligomer destabilization and selectivity for ssDNA. We envision that the interaction between K1543 of the BRC4 and E42 and A44 of the NTD (Figure 2) guide the peptide into the cleft between NTD and the RAD51 core and simultaneously shift the position of the NTD (Figure 1C and D, Supplementary Figures S1C and S2C). This allows placement of the F1546 of the peptide in the hydrophobic pocket within the RAD51 core revealed by the crystal structure. Two hydrogen bonds accepted by E59 from N1544 and K1549 further stabilize the peptide in the cleft between the NTD and the RAD51 core. The peptide then interacts with the S233, which belongs to the Loop1 (dsDNA-binding loop) of the adjacent RAD51 monomer. Notably, cross-subunit interaction appears important for regulating the consequences of BRC4–RAD51 interaction: it stabilizes the interface between two RAD51 monomers in the presence of the peptide.

Another notable interaction is the hydrogen bond between Q1551 of the peptide and P56 within the NTD of RAD51. This interaction positions the C-terminus of the BRC4 peptide near the N terminus of the peptide docked in the second monomer.

The difference between the yeast and human RAD51 proteins in the position and structure of the NTD provides a glimpse into co-evolution of the recombinase and recombination mediator. The more rigid connector between the two domains of human RAD51 shifts the position of NTD relative to the core and creates the binding site that has enough flexibility to accommodate diverse BRC peptides of BRCA2 and other modulators of HR. Notably, BRCA2 is not found in yeast, where Rad52 is the main recombination mediator (10,73). Not surprisingly, the cleft between the Rad51 core and its NTD is too narrow to accommodate the BRC peptide.

Although, the overall extended filamentous structure and DNA strand exchange function is highly conserved within the RecA/RAD51 family of recombinases (74), the important features of their structures and mechanisms differ between species. Understanding of the RAD51 structure within the dynamic nucleoprotein filament may greatly facilitate rational discovery of small-molecule scaffolds, which can be developed into potentially effective anticancer treatments and highly specific molecular probes. It also will improve our understanding of the mechanisms by which the recombination mediators and anti-recombinases affect RAD51 interaction with ssDNA and dsDNA, nucleoprotein filament assembly, disassembly and dynamics.

The *in silico* and *in vitro* studies presented herein complete the BRC4 pharmacophore model of RAD51, as evidenced by the strong correlation between experimental data and MD-based free energy calculations, and provides a basis for initiating structure-based drug discovery against this important antineoplastic target. A number of recent successes in using structure-based discovery of small molecules to rationalize the modulation of protein/protein and protein/peptide complexation (75,76) underscore the potential impact of the current study.

SUPPLEMENTARY DATA

Supplementary Data are available at NAR Online, including [77].

ACKNOWLEDGEMENTS

pChaperone and pET11b/RAD51 vectors were a generous gift from Dr Alex Mazin. M.S., M.A.S. and S.S. designed research; S.S., W.T.J. and M.S. performed experiments; M.A.S. performed computational studies; S.S., W.T.J., M.A.S. and M.S. analyzed data; M.S., M.A.S. and S.S. wrote the article.

FUNDING

Howard Hughes Medical Institute (HHMI) Early Career Scientist award and American Cancer Society

[RSG-09-182-01-DMC to M.S.]; Center for the Physics of Living Cells, University of Illinois at Urbana-Champaign (in part to S.S.); NIH Grant [GM097373 to M.A.S.]. Funding for open access charge: NIH Grant [GM097373].

Conflict of interest statement. None declared.

REFERENCES

1. Amunugama,R., Fishel,R. and Paul,W.D. (2012) In: Doetsch,P.W. (ed.), *Progress in Molecular Biology and Translational Science*, Vol. 110. Academic Press, Oxford, UK, pp. 155–206.
2. Holloman,W.K. (2011) Unraveling the mechanism of BRCA2 in homologous recombination. *Nat. Struct. Mol. Biol.*, **18**, 748–754.
3. Costanzo,V. (2011) Brca2, Rad51 and Mre11: performing balancing acts on replication forks. *DNA Repair*, **10**, 1060–1065.
4. Li,X. and Heyer,W.D. (2008) Homologous recombination in DNA repair and DNA damage tolerance. *Cell Res.*, **18**, 99–113.
5. Oganesian,L. and Karlseder,J. (2011) Mammalian 5′ C-rich telomeric overhangs are a mark of recombination-dependent telomere maintenance. *Mol. Cell*, **42**, 224–236.
6. Ciccia,A. and Elledge,S.J. (2010) The DNA damage response: making it safe to play with knives. *Mol. Cell*, **40**, 179–204.
7. Moynahan,M.E. and Jasin,M. (2010) Mitotic homologous recombination maintains genomic stability and suppresses tumorigenesis. *Nat. Rev. Mol. Cell Biol.*, **11**, 196–207.
8. Holthausen,J.T., Wyman,C. and Kanaar,R. (2011) Regulation of DNA strand exchange in homologous recombination. *DNA Repair*, **9**, 1264–1272.
9. Maher,R.L., Branagan,A.M. and Morrical,S.W. (2011) Coordination of DNA replication and recombination activities in the maintenance of genome stability. *J. Cell. Biochem.*, **112**, 2672–2682.
10. Heyer,W.D., Ehmsen,K.T. and Liu,J. (2010) Regulation of homologous recombination in eukaryotes. *Ann. Rev. Genet.*, **44**, 113–139.
11. Jensen,R.B., Carreira,A. and Kowalczykowski,S.C. (2010) Purified human BRCA2 stimulates RAD51-mediated recombination. *Nature*, **467**, 678–683.
12. Liu,J., Doty,T., Gibson,B. and Heyer,W.D. (2010) Human BRCA2 protein promotes RAD51 filament formation on RPA-covered single-stranded DNA. *Nat. Struct. Mol. Biol.*, **17**, 1260–1262.
13. Thorslund,T., McIlwraith,M.J., Compton,S.A., Lekomtsev,S., Petronczki,M., Griffith,J.D. and West,S.C. (2010) The breast cancer tumor suppressor BRCA2 promotes the specific targeting of RAD51 to single-stranded DNA. *Nat. Struct. Mol. Biol.*, **17**, 1263–1265.
14. Turner,N., Tutt,A. and Ashworth,A. (2004) Hallmarks of 'BRCAness' in sporadic cancers. *Nat. Rev. Cancer*, **4**, 814–819.
15. Nathanson,K.L., Wooster,R. and Weber,B.L. (2001) Breast cancer genetics: what we know and what we need. *Nat. Med.*, **7**, 552–556.
16. Chen,P.L., Chen,C.F., Chen,Y., Xiao,J., Sharp,Z.D. and Lee,W.H. (1998) The BRC repeats in BRCA2 are critical for RAD51 binding and resistance to methyl methanesulfonate treatment. *Proc. Natl Acad. Sci. USA*, **95**, 5287–5292.
17. Bignell,G., Micklem,G., Stratton,M.R., Ashworth,A. and Wooster,R. (1997) The BRC Repeats are Conserved in Mammalian BRCA2 Proteins. *Hum. Mol. Genet.*, **6**, 53–58.
18. Bork,P., Blomberg,N. and Nilges,M. (1996) Internal repeats in the BRCA2 protein sequence. *Nat. Genet.*, **13**, 22–23.
19. Carreira,A. and Kowalczykowski,S.C. (2011) Two classes of BRC repeats in BRCA2 promote RAD51 nucleoprotein filament function by distinct mechanisms. *Proc. Natl Acad. Sci. USA*, **108**, 10448–10453.
20. Islam,M.N., Paquet,N., Fox,D., Dray,E., Zheng,X.F., Klein,H., Sung,P. and Wang,W. (2012) A variant of the breast cancer type 2 susceptibility protein (BRC) repeat is essential for the RECQL5 helicase to interact with RAD51 recombinase for genome stabilization. *J. Biol. Chem.*, **287**, 23808–23818.
21. Spies,M. and Kowalczykowski,S.C. (2006) The RecA binding locus of RecBCD is a general domain for recruitment of DNA strand exchange proteins. *Mol. Cell*, **21**, 573–580.
22. Pellegrini,L., Yu,D.S., Lo,T., Anand,S., Lee,M., Blundell,T.L. and Venkitaraman,A.R. (2002) Insights into DNA recombination from the structure of a RAD51-BRCA2 complex. *Nature*, **420**, 287–293.
23. Nomme,J., Renodon-Corniere,A., Asanomi,Y., Sakaguchi,K., Stasiak,A.Z., Stasiak,A., Norden,B., Tran,V. and Takahashi,M. (2011) Design of potent inhibitors of human RAD51 recombinase based on BRC motifs of BRCA2 protein: modeling and experimental validation of a chimera peptide. *J. Med. Chem.*, **53**, 5782–5791.
24. Scott,D.E., Ehebauer,M.T., Pukala,T., Marsh,M., Blundell,T.L., Venkitaraman,A.R., Abell,C. and Hyvönen,M. (2013) Using a fragment-based approach to target protein–protein interactions. *Chem. Bio. Chem.*, **14**, 332–342.
25. Conway,A.B., Lynch,T.W., Zhang,Y., Fortin,G.S., Fung,C.W., Symington,L.S. and Rice,P.A. (2004) Crystal structure of a Rad51 filament. *Nat. Struct. Mol. Biol.*, **11**, 791–796.
26. Molecular Operating Environment (MOE) 2010.09, C.C.G.I., 1010 Sherbooke St. West, Suite 910, Montreal, QC, Canada, H3A 2R7. (2012).
27. Xing,X. and Bell,C.E. (2004) Crystal structures of *Escherichia coli* RecA in complex with MgADP and MnAMP-PNP. *Biochemistry*, **43**, 16142–16152.
28. Labute,P. (2010) LowModeMD—implicit low-mode velocity filtering applied to conformational search of macrocycles and protein loops. *J. Chem. Inf. Model.*, **50**, 792–800.
29. Darden,T., York,D. and Pedersen,L. (1993) Particle Mesh Ewald-an N.Log(N) method for ewald sums in large systems. *J. Chem. Phys.*, **98**, 10089–10092.
30. Essmann,U., Perera,L., Berkowitz,M.L., Darden,T., Lee,H. and Pedersen,L.G. (1995) A smooth particle mesh ewald method. *J. Chem. Phys.*, **103**, 8577–8593.
31. Jakalian,A., Jack,D.B. and Bayly,C.I. (2002) Fast, efficient generation of high-quality atomic charges. AM1-BCC model: II. parameterization and validation. *J. Comput. Chem.*, **23**, 1623–1641.
32. Hooft,R.W., Vriend,G., Sander,C. and Abola,E.E. (1996) Errors in protein structures. *Nature*, **381**, 272.
33. Krieger,E., Nielsen,J.E., Spronk,C.A. and Vriend,G. (2006) Fast empirical pKa prediction by Ewald summation. *J. Mol. Graph. Model.*, **25**, 481–486.
34. Konagurthu,A.S., Whisstock,J.C., Stuckey,P.J. and Lesk,A.M. (2006) MUSTANG: a multiple structural alignment algorithm. *Proteins*, **64**, 559–574.
35. Juffer,A.H., Botta,E.F.F., Vankeulen,B.A.M., Vanderploeg,A. and Berendsen,H.J.C. (1991) The electric-potential of a macromolecule in a solvent - a fundamental approach. *J. Comput. Phys.*, **97**, 144–171.
36. Zauhar,R.J., Morgan,R.S. and Shaw,P.B. (1985) A polarization charge model for the computation of macromolecular electric-fields. *Biophys. J.*, **47**, A21–A21.
37. Steinbrecher,T. and Labahn,A. (2010) Towards accurate free energy calculations in ligand protein-binding studies. *Curr. Med. Chem.*, **17**, 767–785.
38. Schutz,C.N. and Warshel,A. (2001) What are the dielectric "constants" of proteins and how to validate electrostatic models? *Proteins*, **44**, 400–417.
39. Ravindranathan,K., Tirado-Rives,J., Jorgensen,W.L. and Guimarães,C.R.W. (2011) Improving MM-GB/SA scoring through the application of the variable dielectric model. *J. Chem. Theor. Comput.*, **7**, 3859–3865.
40. Sotriffer,C. and Matter,H. (2011) In: Sotriffer,C. (ed.), *Virtual Screening: Principles, Challenges, and Practical Guidelines*. Wiley-VCH Verlag GmbH & Co. KGaA. Weinheim, Germany, pp. 177–221.
41. Cornell,W.D., Cieplak,P., Bayly,C.I., Gould,I.R., Merz,K.M., Ferguson,D.M., Spellmeyer,D.C., Fox,T., Caldwell,J.W. and Kollman,P.A. (1995) A 2nd generation force-field for the simulation of proteins, nucleic-acids, and organic-molecules. *J. Am. Chem. Soc.*, **117**, 5179–5197.

42. Baumann,P., Benson,F.E., Hajibagheri,N. and West,S.C. (1997) Purification of human Rad51 protein by selective spermidine precipitation. *Mutat. Res.*, **384**, 65–72.
43. Henricksen,L.A., Umbricht,C.B. and Wold,M.S. (1994) Recombinant replication protein A: expression, complex formation, and functional characterization. *J. Biol. Chem.*, **269**, 11121–11132.
44. LiCata,V.J. and Wowor,A.J. (2008) Applications of fluorescence anisotropy to the study of protein-DNA interactions. *Methods Cell Biol.*, **84**, 243–262.
45. Carreira,A., Hilario,J., Amitani,I., Baskin,R.J., Shivji,M.K., Venkitaraman,A.R. and Kowalczykowski,S.C. (2010) The BRC repeats of BRCA2 modulate the DNA binding selectivity of RAD51. *Cancer Cell*, **136**, 1032–1043.
46. Grimme,J.M. and Spies,M. (2011) FRET-based assays to monitor DNA binding and annealing by Rad52 recombination mediator protein. *Methods Mol. Biol.*, **745**, 463–483.
47. Pettersen,E.F., Goddard,T.D., Huang,C.C., Couch,G.S., Greenblatt,D.M., Meng,E.C. and Ferrin,T.E. (2004) UCSF chimera—a visualization system for exploratory research and analysis. *J. Comput. Chem.*, **25**, 1605–1612.
48. Krieger,E., Joo,K., Lee,J., Lee,J., Raman,S., Thompson,J., Tyka,M., Baker,D. and Karplus,K. (2009) Improving physical realism, stereochemistry, and side-chain accuracy in homology modeling: Four approaches that performed well in CASP8. *Proteins*, **77**, 114–122.
49. Reymer,A., Frykholm,K., Morimatsu,K., Takahashi,M. and Norden,B. (2009) Structure of human Rad51 protein filament from molecular modeling and site-specific linear dichroism spectroscopy. *Proc. Natl Acad. Sci. USA*, **106**, 13248–13253.
50. Matsuo,Y., Sakane,I., Takizawa,Y., Takahashi,M. and Kurumizaka,H. (2006) Roles of the human Rad51 L1 and L2 loops in DNA binding. *FEBS J.*, **273**, 3148–3159.
51. Bugreev,D.V. and Mazin,A.V. (2004) Ca2+ activates human homologous recombination protein Rad51 by modulating its ATPase activity. *Proc. Natl Acad. Sci. USA*, **101**, 9988–9993.
52. Ristic,D., Modesti,M., van der Heijden,T., van Noort,J., Dekker,C., Kanaar,R. and Wyman,C. (2005) Human Rad51 filaments on double- and single-stranded DNA: correlating regular and irregular forms with recombination function. *Nucleic Acids Res.*, **33**, 3292–3302.
53. Grimme,J.M., Honda,M., Wright,R., Okuno,Y., Rothenberg,E., Mazin,A.V., Ha,T. and Spies,M. (2010) Human Rad52 binds and wraps single-stranded DNA and mediates annealing via two hRad52-ssDNA complexes. *Nucleic Acids Res.*, **38**, 2917–2930.
54. Masuda-Ozawa,T., Hoang,T., Seo,Y.S., Chen,L.F. and Spies,M. (2013) Single-molecule sorting reveals how ubiquitylation affects substrate recognition and activities of FBH1 helicase. *Nucleic Acids Res.*, **41**, 3576–3587.
55. Davies,A.A., Masson,J.Y., McIlwraith,M.J., Stasiak,A.Z., Stasiak,A., Venkitaraman,A.R. and West,S.C. (2001) Role of BRCA2 in control of the RAD51 recombination and DNA repair protein. *Mol. Cell*, **7**, 273–282.
56. Davies,O.R. and Pellegrini,L. (2007) Interaction with the BRCA2 C terminus protects RAD51-DNA filaments from disassembly by BRC repeats. *Nat. Struct. Mol. Biol.*, **14**, 475–483.
57. Nomme,J., Takizawa,Y., Martinez,S.F., Renodon-Cornière,A., Fleury,F., Weigel,P., Yamamoto,K.I., Kurumizaka,H. and Takahashi,M. (2008) Inhibition of filament formation of human Rad51 protein by a small peptide derived from the BRC-motif of the BRCA2 protein. *Genes Cells*, **13**, 471–481.
58. Carreira,A., Hilario,J., Amitani,I., Baskin,R.J., Shivji,M.K., Venkitaraman,A.R. and Kowalczykowski,S.C. (2009) The BRC repeats of BRCA2 modulate the DNA-binding selectivity of RAD51. *Cell*, **136**, 1032–1043.
59. Cole,D.J., Rajendra,E., Roberts-Thomson,M., Hardwick,B., McKenzie,G.J., Payne,M.C., Venkitaraman,A.R. and Skylaris,C.K. (2011) Interrogation of the protein-protein interactions between human BRCA2 BRC repeats and RAD51 reveals atomistic determinants of affinity. *PLoS Comput. Biol.*, **7**, e1002096.
60. Brown,S.P. and Muchmore,S.W. (2009) Large-scale application of high-throughput molecular mechanics with Poisson-Boltzmann surface area for routine physics-based scoring of protein-ligand complexes. *J. Med. Chem.*, **52**, 3159–3165.
61. Shirts,M.R., Mobley,D.L. and Brown,S.P. (2010) *Drug design:structure- and ligand-based approaches*. Cambridge University Press, Cambridge, U.K; New York.
62. Pal,J., Bertheau,R., Buon,L., Qazi,A., Batchu,R.B., Bandyopadhyay,S., Ali-Fehmi,R., Beer,D.G., Weaver,D.W., Reis,R.S. *et al.* (2011) Genomic evolution in Barrett's adenocarcinoma cells: critical roles of elevated hsRAD51, homologous recombination and Alu sequences in the genome. *Oncogene*, **30**, 3585–3598.
63. Shammas,M.A., Shmookler Reis,R.J., Koley,H., Batchu,R.B., Li,C. and Munshi,N.C. (2009) Dysfunctional homologous recombination mediates genomic instability and progression in myeloma. *Blood*, **113**, 2290–2297.
64. Slupianek,A., Dasgupta,Y., Ren,S.Y., Gurdek,E., Donlin,M., Nieborowska-Skorska,M., Fleury,F. and Skorski,T. (2011) Targeting RAD51 phosphotyrosine-315 to prevent unfaithful recombination repair in BCR-ABL1 leukemia. *Blood*, **118**, 1062–1068.
65. Short,S.C., Giampieri,S., Worku,M., Alcaide-German,M., Sioftanos,G., Bourne,S., Lio,K.I., Shaked-Rabi,M. and Martindale,C. (2011) Rad51 inhibition is an effective means of targeting DNA repair in glioma models and CD133+ tumor derived cells. *Neuro Oncol.*, **13**, 487–499.
66. Qiao,G.B., Wu,Y.L., Yang,X.N., Zhong,W.Z., Xie,D., Guan,X.Y., Fischer,D., Kolberg,H.C., Kruger,S. and Stuerzbecher,H.W. (2005) High-level expression of Rad51 is an independent prognostic marker of survival in non-small-cell lung cancer patients. *Br. J. Cancer*, **93**, 137–143.
67. Huang,F., Mazina,O.M., Zentner,I.J., Cocklin,S. and Mazin,A.V. (2012) Inhibition of homologous recombination in human cells by targeting RAD51 recombinase. *J. Med. Chem.*, **55**, 3011–3020.
68. Huang,F., Motlekar,N.A., Burgwin,C.M., Napper,A.D., Diamond,S.L. and Mazin,A.V. (2011) Identification of specific inhibitors of human RAD51 recombinase using high-throughput screening. *ACS Chem. Biol.*, **6**, 628–635.
69. Jayathilaka,K., Sheridan,S.D., Bold,T.D., Bochenska,K., Logan,H.L., Weichselbaum,R.R., Bishop,D.K. and Connell,P.P. (2008) A chemical compound that stimulates the human homologous recombination protein RAD51. *Proc. Natl Acad. Sci. USA*, **105**, 15848–15853.
70. Martinez,S.F., Renodon-Corniere,A., Nomme,J., Eveillard,D., Fleury,F., Takahashi,M. and Weigel,P. (2011) Targeting human Rad51 by specific DNA aptamers induces inhibition of homologous recombination. *Biochimie*, **92**, 1832–1838.
71. Budke,B., Logan,H.L., Kalin,J.H., Zelivianskaia,A.S., Cameron McGuire,W., Miller,L.L., Stark,J.M., Kozikowski,A.P., Bishop,D.K. and Connell,P.P. (2012) RI-1: a chemical inhibitor of RAD51 that disrupts homologous recombination in human cells. *Nucleic Acids Res.*, **40**, 7347–7357.
72. Surade,S. and Blundell,T.L. (2012) Structural biology and drug discovery of difficult targets: the limits of ligandability. *Chem. Biol.*, **19**, 42–50.
73. Liu,J. and Heyer,W.D. (2011) Who's who in human recombination: BRCA2 and RAD52. *Proc. Natl Acad. Sci. USA*, **108**, 441–442.
74. Liu,J., Ehmsen,K.T., Heyer,W.D. and Morrical,S.W. (2011) Presynaptic filament dynamics in homologous recombination and DNA repair. *Crit. Rev. Biochem. Mol. Biol.*, **46**, 240–270.
75. Metz,A., Pfleger,C., Kopitz,H., Pfeiffer-Marek,S., Baringhaus,K.H. and Gohlke,H. (2011) Hot spots and transient pockets: predicting the determinants of small-molecule binding to a protein–protein interface. *J. Chem. Inf. Model.*, **52**, 120–133.
76. Eyrisch,S. and Helms,V. (2009) What induces pocket openings on protein surface patches involved in protein–protein interactions? *J Comput. Aided. Mol. Des.*, **23**, 73–86.
77. Whitmore,L. and Wallace,B.A. (2004) DICHROWEB, an online server for protein secondary structure analyses from circular dichroism spectroscopic data. *Nucleic Acids Res.*, **32**, W668–W673.